

Temporal subtraction of low-dose and relatively thick-slice CT images with large deformation diffeomorphic metric mapping and adaptive voxel matching for detection of bone metastases

A STARD-compliant article

Mitsuteru Tsuchiya, MD^{a,*}, Takayuki Masui, MD, PhD^b, Motoyuki Katayama, MD, PhD^b, Yuki Hayashi, MD^b, Takahiro Yamada, MD^b, Kazuma Terauchi, MD^b, Kenshi Kawamura, MD^b, Ryo Ishikawa, PhD^c, Hideaki Mizobe, MS^c, Junta Yamamichi, MS, MPH^c, Harumi Sakahara, MD, PhD^d, Satoshi Goshima, MD, PhD^d

Abstract

To evaluate the improvement of radiologist performance in detecting bone metastases at follow up low-dose computed tomography (CT) by using a temporal subtraction (TS) technique based on an advanced nonrigid image registration algorithm.

Twelve patients with bone metastases (males, 5; females, 7; mean age, 64.8 ± 7.6 years; range 51–81 years) and 12 control patients without bone metastases (males, 5; females, 7; mean age, 64.8 ± 7.6 years; 51–81 years) were included, who underwent initial and follow-up CT examinations between December 2005 and July 2016. Initial CT images were registered to follow-up CT images by the algorithm, and TS images were created. Three radiologists independently assessed the bone metastases with and without the TS images. The reader averaged jackknife alternative free-response receiver operating characteristics figure of merit was used to compare the diagnostic accuracy.

The reader-averaged values of the jackknife alternative free-response receiver operating characteristics figures of merit (θ) significantly improved from 0.687 for the readout without TS and 0.803 for the readout with TS (P value = .031. F statistic = 5.24). The changes in the absolute value of CT attenuations in true-positive lesions were significantly larger than those in false-negative lesions ($P < .001$). Using TS, segment-based sensitivity, specificity, accuracy, positive predictive value, and negative predictive value of the readout with TS were 66.7%, 98.9%, 94.4%, 90.9%, and 94.8%, respectively.

The TS images can significantly improve the radiologist's performance in the detection of bone metastases on low-dose and relatively thick-slice CT.

Abbreviations: 18F = [18F] fluorodeoxyglucose (FDG), CAD = computer-aided detection, CT = computed tomography, FN = false negative, FP = false positive, JAFROC = jackknife alternative free-response receiver operating characteristics, LDDMM = large deformation diffeomorphic metric mapping, MRI = magnetic resonance imaging, PET = positron emission tomography, TP = true positive, TS = temporal subtraction.

Keywords: computer-assisted diagnosis, multidetector computed tomography, neoplasm metastases, positron emission tomography-computed tomography, sensitivity and specificity, subtraction technique

Editor: N/A.

M.T., T.M., M.K., Y.H., T.Y., K.T., K.K., H.S., and S.G. declare no relationships with any companies, whose products or services may be related to the subject matter of the article.

R.I., H.M and J.Y. are Canon employees.

^a Department of Diagnostic Radiology and Nuclear Medicine, Graduate School of Medicine, Hamamatsu University School of Medicine, 1-20-1 Handayama, Higashi-ku,

^b Department of Radiology, Seirei Hamamatsu General Hospital, 2-12-12, Sumiyoshi, Naka-ku, Hamamatsu City, Shizuoka, ^c Medical Imaging Information Technology Development Department Canon Inc.70-1, Yanagi-cho, Saiwai-ku, Kawasaki-shi, Kanagawa, ^d Department of Diagnostic Radiology and Nuclear Medicine, Hamamatsu University School of Medicine, 1-20-1 Handayama, Higashi-ku, Hamamatsu City, Shizuoka, Japan.

* Correspondence: Mitsuteru Tsuchiya, Graduate School of Medicine, Hamamatsu University School of Medicine, Hamamatsu, Shizuoka, Japan (e-mail: d16018@hama-med.ac.jp).

Copyright © 2020 the Author(s). Published by Wolters Kluwer Health, Inc.

This is an open access article distributed under the terms of the Creative Commons Attribution-Non Commercial License 4.0 (CCBY-NC), where it is permissible to download, share, remix, transform, and buildup the work provided it is properly cited. The work cannot be used commercially without permission from the journal.

How to cite this article: Tsuchiya M, Masui T, Katayama M, Hayashi Y, Yamada T, Terauchi K, Kawamura K, Ishikawa R, Mizobe H, Yamamichi J, Sakahara H, Goshima S. Temporal subtraction of low-dose and relatively thick-slice CT images with large deformation diffeomorphic metric mapping and adaptive voxel matching for detection of bone metastases: a STARD-compliant article. *Medicine* 2020;99:12(e19538).

Received: 1 August 2019 / Received in final form: 11 February 2020 / Accepted: 13 February 2020

<http://dx.doi.org/10.1097/MD.00000000000019538>

1. Introduction

Bone is the most common site to which many types of cancers metastasize.^[1] Breast cancer and prostate cancer have the highest frequency of bone metastasis, followed by cancer of the lung, colon, stomach, bladder, uterus, rectum, thyroid, or kidney.^[2,3] It is estimated that over 400,000 individuals are affected by bone metastasis in the United States annually.^[4] Skeletal-related events due to bone metastases can include pain, pathologic fracture, hypercalcemia, spinal cord or nerve root compression, and spinal instability.^[2] Therefore, early detection and treatment to preserve quality of life should be considered.^[5,6]

Computed tomography (CT) of the chest, abdomen, and pelvis is widely available and plays a vital role in the diagnosis and staging of almost all types of cancer.^[7–10] According to the meta-analysis, for the detection of the vertebral metastases, on per-patient based and per-lesion based sensitivity of CT was significantly lower than that of positron emission tomography (PET), single photon emission computed tomography (SPECT), magnetic resonance imaging (MRI), and bone scintigraphy.^[11] For CT evaluation, bone metastases can be easily overlooked by radiologists, especially when bone windows are underused.^[3]

The need for a diagnostic tool that helps radiologists has resulted in the development of computer-aided detection (CAD). CAD can increase the accuracy of diagnosis and shortens the time required for diagnosis. An example of CAD is temporal subtraction (TS) that emphasizes bone lesions.^[12–15]

Several reports have examined the detection of bone lesions using a TS method with thinner slice CT, such as 1.0 mm or less.^[13–15] However, in general, a CT examination of the abdomen and the pelvis includes transaxial images with a slice thickness of 5 mm or less, as stated by the relevant American College of Radiology (ACR) practice parameter.^[16] The evaluation of CT images with slice thickness values of 1.0 mm or less has not been generalized yet in routine clinical practices. Thicker slices are used more frequently for numerous clinical indications. Therefore, the detection rate of bone metastasis by the TS method with slices thicker than 1.0 mm should be evaluated.

A TS method for the detection of bone metastases on CT images with thinner slices (1.0 or 0.5 mm) and using large deformation diffeomorphic metric mapping (LDDMM) for a non-rigid image registration resulted in improved outcomes.^[13–15] LDDMM uses a cascade process to correct the large displacement between the 2 corresponding images.^[17,18] TS of thicker slices is challenging because of misregistration and partial volume effects. In this study, to reduce the partial volume effects, an algorithm called adaptive voxel matching^[19] was applied.^[20]

18F-fluorodeoxyglucose (FDG) PET/CT is used to detect metastases including bone lesions.^[21] 18F-FDG PET/CT has adequate sensitivity to detect lytic bone metastases; however, sclerotic bone metastases may be difficult to detect, although bone scintigraphy has shown higher sensitivity.^[22] The low-dose CT scanning is used for the CT-based attenuation correction in PET/CT.^[23] TS generated from low-dose CT may provide sensitivity equivalent to that of TS generated from standard-dose CT and improve the detectability of osteoblast lesions in 18F-FDG PET/CT. Therefore, in this study, we used low-radiation dose CT with thicker slices.

The objective of this study was to investigate the feasibility of whether the TS images generated from low-dose and relatively thick-slice CT can be used to improve the ability to detect bone metastatic lesions. We hypothesized that the evaluations with the

TS images generated by LDDMM and AdVM would be more likely to improve radiologist's performance to detect bone metastases compared to the evaluations with only initial CT and follow up CT images.

2. Materials and methods

Institutional review board approval was obtained, and the requirement for written informed consent was waived for this retrospective study. Health Insurance Portability and Accountability Act (HIPAA) compliance was maintained throughout all phases of the current study.

2.1. Patients

A search of the radiology reporting system database was performed. Based on radiological reports in our institution from December 2005 to July 2016, the following patients were selected: patients who underwent low-dose CT for free breathing PET/CT covering the head to the proximal femurs, with 3.75-mm slice thickness, at 2 time points with identical parameters. Among them, bone metastases were newly recognized on the follow-up CT but not at the initial CT. From those patients, 1 patient was excluded because of the 5-year or longer interval between the two CT scans. As a result, 12 patients (males, 5; females, 7; mean age \pm standard deviation (S.D.) = 64.8 ± 7.6 years; range 51–81 years) were selected. As controls without bone metastases, 12 age- and sex- one-to-one matched patients (males, 5; females, 7; 64.8 ± 7.6 years; 51–81 years) with a comparable interval between the 2 CT scans (average 618 days) were selected from the same database. Selection of the patient population was made as follows (Fig. 1).

2.2. Imaging technique

All examinations of the 48 low-dose CT images studies included in our study were performed within our hospital. All PET/CT studies were performed on the same 16-section PET/CT scanner (Discovery STE; GE Healthcare, Waukesha, WI) according to the standard clinical protocol at our institution. The CT scans were obtained to match the PET scan field of view and section thickness. All studies were performed with the patient in a supine position with the arms down. The unenhanced attenuation-correction low-dose CT was obtained with the following technical parameters: tube voltage 140 kVp, tube current-time product of 29 mAs, 20×1.25 mm slice collimation, and spiral pitch of 1.75. Reconstructed section thickness was 3.75 mm, at 512×512 pixels.

2.3. Standard of reference

The standard of reference was established by 2 radiologists (with 18 and 6 years of experience of oncologic CT images), discrepancies between the two reviewers were resolved with consensus. These radiologists used all available clinical information: the original transverse CT images, histopathological results of CT guided biopsy, 18F-FDG PET/CT, contrast-enhanced MRI, and/or bone scintigraphy, with medical records for the verification of diagnosis. The lesion location and type of bone metastases (lytic, sclerotic, mixed, and intertrabecular) were recorded. The CT attenuation of bone metastases were measured (Hounsfield units) using software. Regions of interest (ROIs) were set in lesions of initial CT and follow-up CT images.

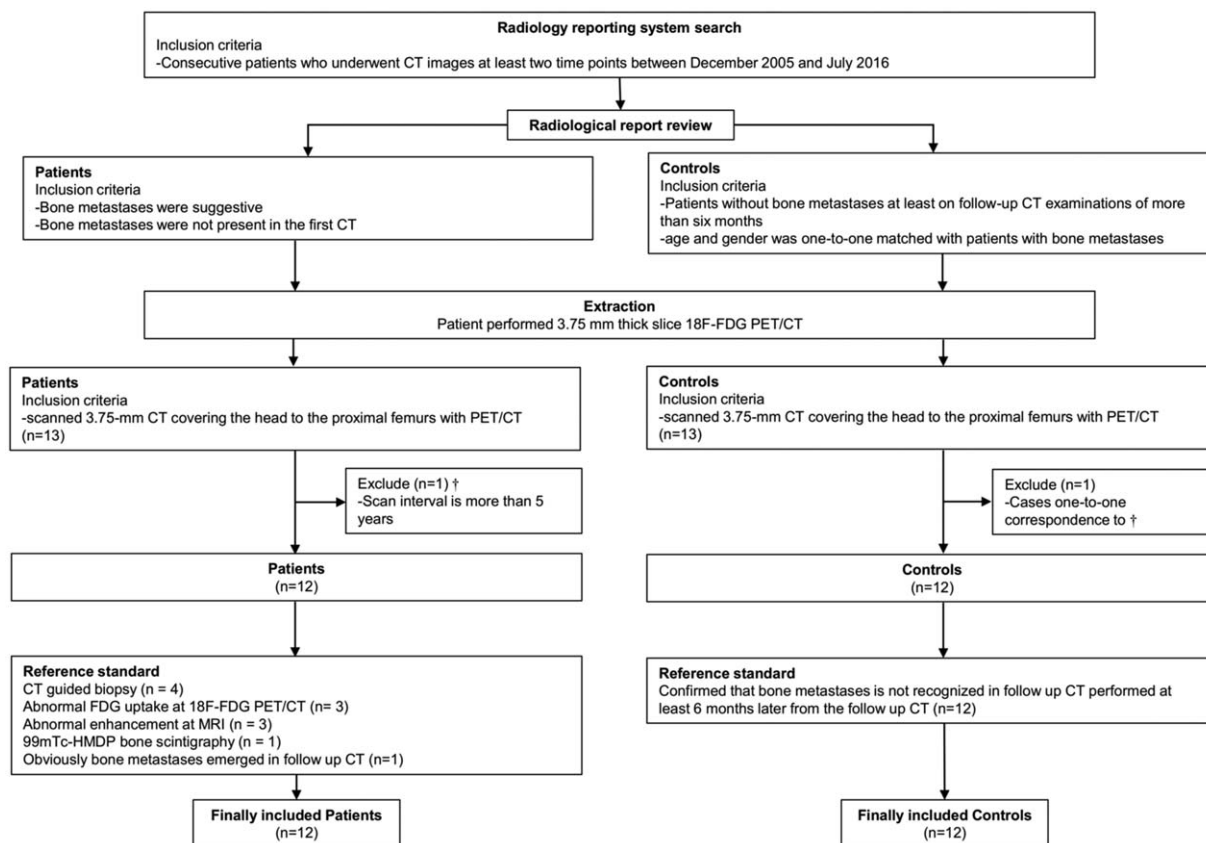


Figure 1. Patient flow chart.

For controls, the absence of bone metastasis confirmed that continued growth was not found on subsequent CT images that were obtained at least 6 months after the initial CT scan from follow-up CT and medical records. In addition, if available, 18F-FDG PET/CT, bone scintigraphy and contrast-enhanced MRI data were used.

2.4. Type of bone metastasis

Lytic: The osteolytic type indicates lesions with decrease in the bone attenuation, or loss of demarcation of the bone structures, with at least 20% lytic voxels in a predominantly sclerotic lesion.^[24] Lytic lesions were further characterized as probable or unlikely metastases; only probable metastases were included in our study. For example, unlikely metastases included Schmorl nodes, areas of degenerative disk disease or osteopenia, and hemangiomas.

Sclerotic: This type had at least 20% sclerotic voxels in a predominantly lytic lesion,^[24] the osteoblastic type indicates lesions with increase in the bone attenuation.

Mixed: The mixed type indicates lesions with features of both the lytic and sclerotic types.

Intertrabecular: Metastatic intertrabecular bone metastases that infiltrate the bone marrow space without trabecular bone alteration are not visible on CT, but cancer invasion to the bone is detectable by avid uptake on 18F-FDG PET/CT and/or abnormal enhancement of MRI.^[25]

2.5. Temporal subtraction

All CT datasets were post-processed with the subtraction algorithm on an off-line computer. This post-processing was fully automated. LDDMM and AdVM were incorporated for the final registration of the CT images.^[19,26,27] An affine transformation was applied prior to LDDMM.^[28] We also used an algorithm called adaptive voxel matching^[19] that reduces the subtraction artifacts from partial volume effects by considering the gaps of the discretized position based on the slice thickness of 2 input images. The TS images were obtained by subtracting transformed initial images from the follow-up images. The details are described in the appendix.

2.6. Image Analysis

Each patient was assigned a random identification number and images were displayed on 23-inch monitors (Flex scan, EV2336W, EIZO) (Fig. 2). The first evaluations of bone metastases were independently made on the pair of initial and follow up CT images without the TS image by three radiologists (with 3, 4, and 29 years of experience in body CT image, respectively) without information of all clinical data, radiological reports, or the reference standard. With an interval of longer than 14 days, second evaluations were made on the pair of CT images with the TS image. The initial and follow up CT images were displayed with a bone window setting (window width 4000 HU; window level 1000 HU), and the TS images were displayed with a

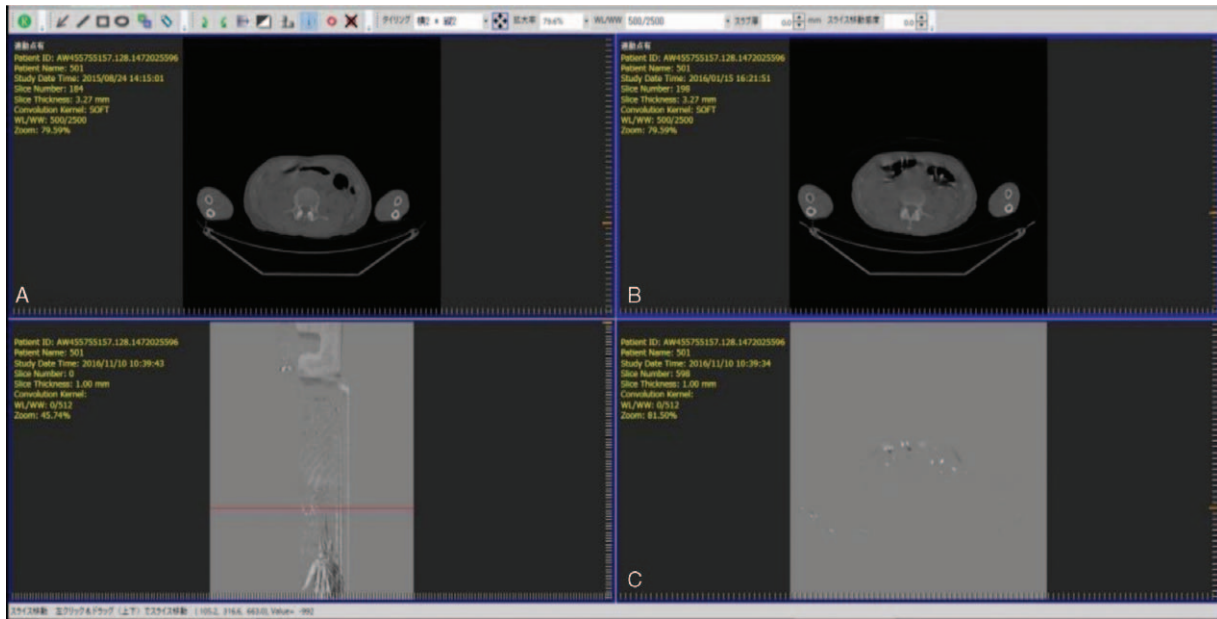


Figure 2. Screenshots of the image viewer for the observer study. A: initial CT, B: follow up CT, C: temporal subtraction image is displayed. CT = computed tomography.

fixed window setting (window width 512 HU; window level 0 HU).

2.6.1. Lesion analysis. The presence of bone metastasis was evaluated using a five-point scale on a lesion-by-lesion basis:

- (1) the lesion was definitely not a bone metastasis;
- (2) the lesion was probably not a bone metastasis;
- (3) the lesion was possibly a bone metastasis;
- (4) the lesion was probably a bone metastasis; and
- (5) the lesion was definitely a bone metastasis.

A score of 4 or 5 would be considered a positive diagnosis. The location of the metastatic lesion was marked and saved as a screen capture. The metastatic lesions were categorized as lytic, sclerotic, mixed, or intertrabecular types.

2.6.2. Segment analysis. The head and body areas were divided into nine segments (head, anterior rib and sternum, posterior rib, cervical vertebra, thoracic vertebra, lumbar vertebra, pelvis, right proximal femur, and left proximal femur).

A true-positive (TP) result was recorded when the location of the bone metastasis, given a confidence score of 4–5, was correctly identified. A false-positive (FP) result was recorded when a bone metastasis-free image had been marked as containing a bone metastasis by the observer or when an image containing a bone metastasis had been marked at a location that was outside of the bone metastasis. A false-negative (FN) result was recorded when a bone metastasis was not (correctly) identified. A true-negative result was recorded when a bone metastasis-free segment has not been marked by the reader.

2.6.3. Image quality. Image quality and registration artifacts on the TS images in each segment were evaluated using a five-point scale (1 poor, not diagnostic to 5 excellent or no artifacts) on a segment-by-segment basis.

2.6.4. Reading time. The mean reading time, per patient, to evaluate images, with and without a TS image, was recorded in all patients.

2.7. Statistical analysis

To analyze and compare the performance of the radiologist with and without TS images for detection of bone metastases, we performed jackknife alternative free-response receiver operating characteristic (JAFROC) analysis using a maximum-likelihood estimation program (JAFROC, version 4.2.1; <http://www.devchakraborty.com>).^[29] Mean diagnostic accuracy was calculated according to the mean figure of merit (θ), which was defined as the probability that on normal images, a lesion is rated higher than the highest-rated non-lesion. The F statistic was used internally for analysis of variance, yielding a *P* value for rejecting the null hypothesis of no difference between the image interpretation sessions.^[30] Due to the limited numbers of readers, only results for fixed reader random case are reported. The clinical background (age and scan interval) of the patients with and without bone metastases was compared by the Mann–Whitney *U* test in each group. One-way analysis of variance with the Games-Howell post hoc test was used to compare the image quality scores between each segment. The Wilcoxon signed rank test was used for significance testing of reading time. Two-way mixed-model intraclass correlation coefficients were used to assess the agreement among the three readers of the segment-based confidence level in all the CT evaluations. Agreement based on intraclass correlation coefficients was classified using the following definitions: 0–0.39, poor; 0.40–0.59, fair; 0.60–0.74, good; and 0.75–1.0, excellent.^[31] *P* values of less than .05 were considered statistically significant. Data analysis was performed using R version 3.3.0 (R Foundation for Statistical Computing, Vienna, Austria), RJafroc version 1.0.2 (<https://cran.r-project.org/web/packages/RJafroc/index.html>), and SPSS version 24

Table 1
Demographics in the patient and control groups.

	Patients	Controls	P value
Male:female	5:7	5:7	—
Age (years)	64.75 ± 7.56*	64.75 ± 7.56*	*1.00
Range	51–81	51–81	
Follow up period (days)	618 ± 500*	683 ± 418*	.590
Range	115–1503	73–1639	

*Numbers indicate average number ± standard deviation.

(IBM Corp., Armonk, NY), and JAFROC (version 4.2.1; <http://www.devchakraborty.com>).

3. Results

3.1. Demographics of the patients and lesion characteristics

Twenty-four patients were included in this study: 12 patients with bone metastases detected at follow-up CT (7 women, 5 men; mean age ± SD, 64.75 ± 7.56 years) and 12 controls without bone

metastases (7 women, 5 men; mean age ± SD, 64.75 ± 7.56 years). Twelve patients had 45 bone metastases in the head to the proximal femurs. The diagnosis of bone metastasis was verified by CT-guided biopsy (n = 4), 18F-FDG PET/CT (n = 3), contrast-enhanced MRI (n = 3), and/or bone scintigraphy (n = 1), and the obvious appearance of a bone lesion in follow-up CT (n = 1). There was no statistically significant difference in demographics between the patient group and control group (Table 1). Of the 12 positive cases, 6 (50.0%) were lung carcinoma, 2 (16.7%) were breast carcinoma, 1 (8.3%) was hypopharynx cancer, 1 (8.3%) was bladder carcinoma, 1 (8.3%) was endometrial stromal sarcoma, and 1 (8.3%) was ovarian serous cystadenocarcinoma. With regard to the standard of reference, the median number of bone metastases per patient was 3.8.

3.2. The appearance of TS images

Depending on the type of lesion, the appearance of bone metastases on TS images varied. Lytic metastases appeared as areas of low signal intensity on TS images (Fig. 3A). Sclerotic metastases appeared as areas of high signal intensity (Fig. 3B). Mixed metastases had a heterogeneous appearance, with areas of low and high signal intensity (Fig. 3C).

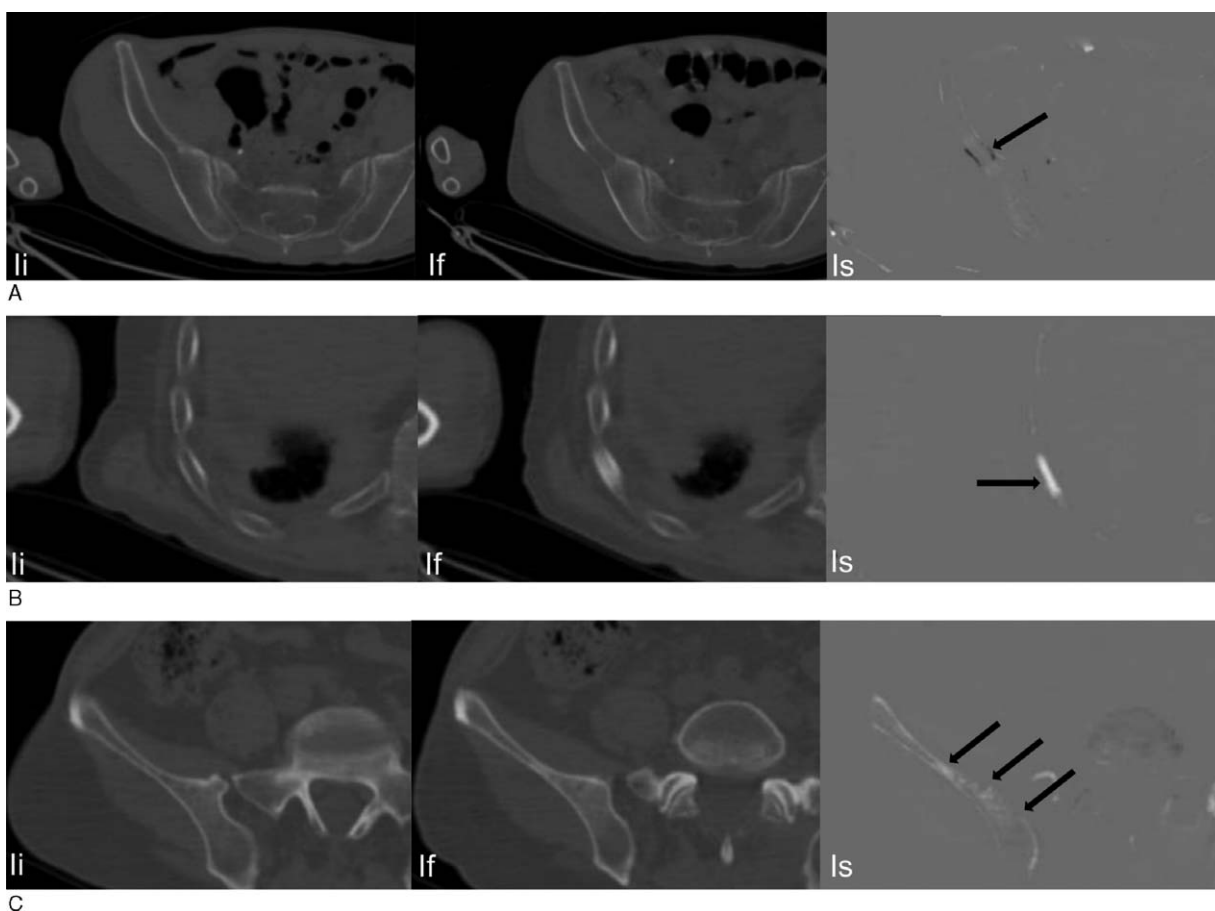


Figure 3. Lytic, Sclerotic, Mixed bone metastases in TS image. The TS images generated from the 3.75 mm CT images. The TS images indicate the bone metastases (arrows) with various appearances (li, initial CT images; lf, follow up CT images; ls, TS images). (A) A case of a 70-year-old man with a history of lung cancer with an osteolytic lesion in the right ilium. The osteolytic lesion appears as hypointense on the TS image. (B) A case of a 64-year-old man with a history of lung cancer with an osteoblastic lesion in the 6th right rib. The osteoblastic lesion appears as hyperintense on the TS image. (C) A case of a 64-year-old man with a history of lung cancer with a mixed osteolytic and osteoblastic lesion in the right ilium. The mixed osteolytic and osteoblastic lesion has a heterogeneous intensity on the TS image. CT = computed tomography, TS = temporal subtraction.

	Without TS	With TS	P
Reader 1	$\theta=0.780$	$\theta=0.866$	$P=.1487$
Reader 2	$\theta=0.706$	$\theta=0.798$	$P=.1487$
Reader 3	$\theta=0.575$	$\theta=0.745$	$P=.0945$
Average	$\theta=0.687$	$\theta=0.803$	$P=.0308$

Note - θ is the JAFROC figures of merit.

JAFROC = jackknife alternative free-response receiver operating characteristics.

3.3. Diagnostic performance

The diagnostic performance with and without TS for the detection of bone metastases in terms of the figure of merit (θ) determined using JAFROC analysis is presented in Table 2. The reader-averaged values of the JAFROC figures of merit (θ) was 0.687 for the readout without TS and 0.803 for the readout with TS. In addition, the 95% confidence interval for $\Delta\theta$ (the difference in the figures of merit between the 2 readout) was -0.221 to -0.116 . JAFROC analysis indicated that the difference between the readout with TS and the readout without TS was significant for the detection of bone metastases at the 5% level (P value = .0308, F statistic = 5.24) (Fig. 4).

3.4. Measurement of CT attenuation of bone metastasis lesions

When the average CT attenuations of the bone metastases in the initial CT and the follow-up CT were compared, it was found that

84.6 H.U. was decreased in the lytic lesions, 362.6 H.U. increased in the sclerotic lesions, 75.6 H.U. in the mixed lesions, and 8.3 H.U. in the intertrabecular lesions. The average changes in the absolute value of the CT attenuations of bone metastases from the initial CT to the follow-up CT were 194.2 H.U. for TP lesions marked in TS and 78.1 H.U. for FN lesions in TS. The changes in absolute value of CT attenuations in TP lesions were significantly larger than those in FN lesions ($P < .001$) (Fig. 5).

3.5. Segment-based and Patient-based sensitivity, specificity, accuracy, positive predictive value, and negative predictive value

In segment-based analysis, sensitivity, specificity, accuracy, positive predictive value, and negative predictive value of the readout without TS were 54.5% (95% CI, 43.6%–65.0%), 98.7% (95% CI, 97.4%–99.5%), 92.6% (95% CI, 90.3%–94.5%), 87.5% (95% CI, 75.9%–94.8%), and 93.1% (95% CI, 90.7%–95.0%), respectively. Sensitivity, specificity, accuracy, positive predictive value, and negative predictive value of the readout with TS were 66.7% (95% CI, 55.9%–76.3%), 98.9% (95% CI, 97.7%–99.6%), 94.4% (95% CI, 92.4%–96.1%), 90.9% (95% CI, 81.3%–96.6%), and 94.8% (95% CI, 92.7%–96.5%), respectively (Table 3).

In patient-based analysis, sensitivity, specificity, accuracy, positive predictive value, and negative predictive value of the readout without TS were 66.7% (95% CI, 49.0%–81.4%), 91.7% (95% CI, 77.5%–98.2%), 79.2% (95% CI, 68.0%–87.8%), 88.9% (95% CI, 70.8%–97.6%), and 73.3% (95% CI,

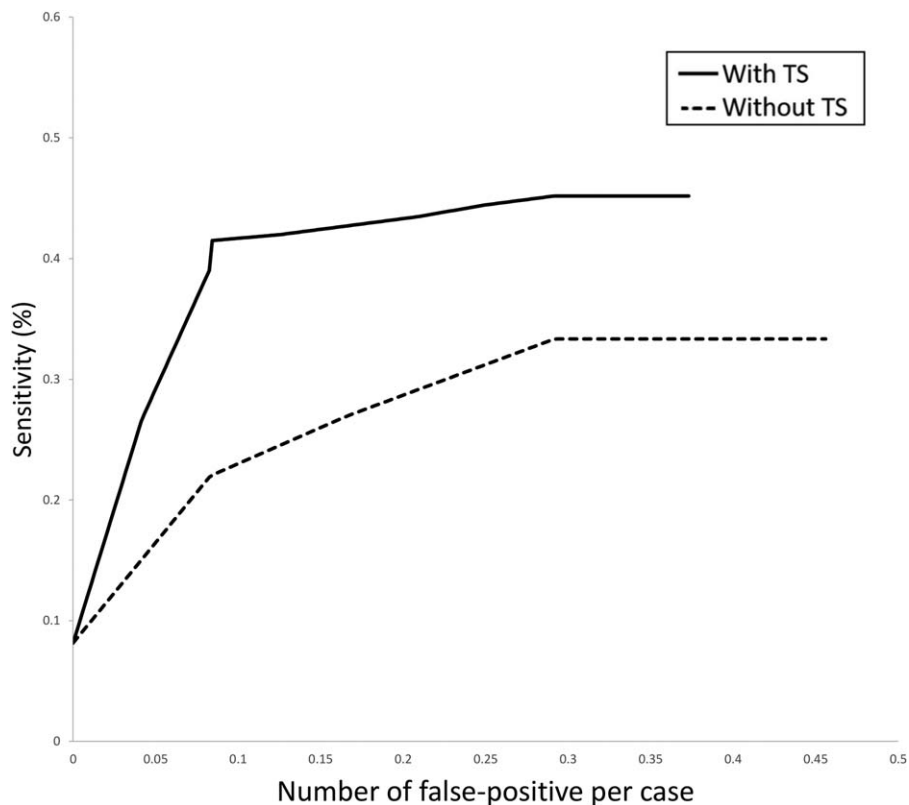


Figure 4. Average free-response receiver operating characteristic curves without (dotted line) and with (solid line) temporal subtraction images. Radiologist performance significantly improved with temporal subtraction images ($P = .0308$).

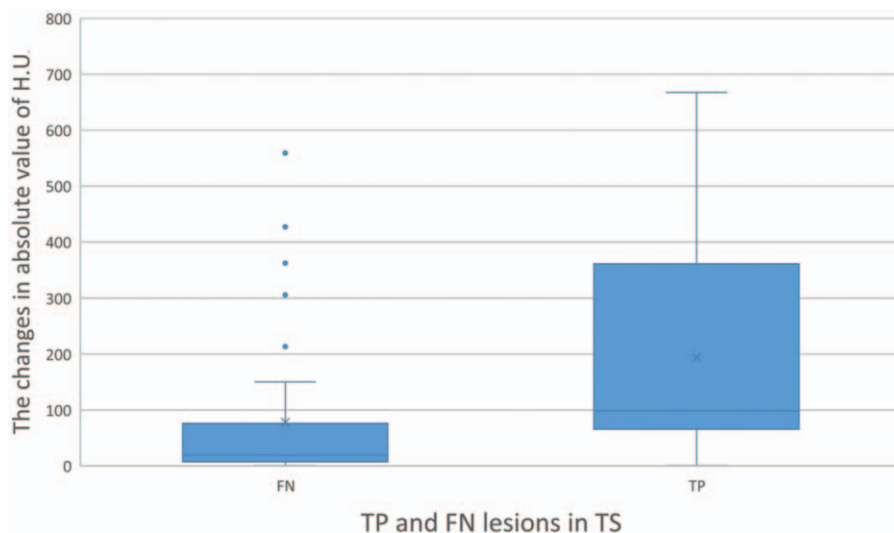


Figure 5. The HU change of TP and FN bone metastases lesion in temporal subtraction. The change in the absolute value of HU from initial CT to follow up CT of TP lesion was significantly larger than that of FN lesion ($P < .001$). HU = Hounsfield unit, FN = false negative, TP = true positive,

58.1%–85.4%), respectively. Sensitivity, specificity, accuracy, positive predictive value, and negative predictive value of the readout with TS were 86.1% (95% CI, 70.5%–95.3%), 91.7% (95% CI, 77.5%–98.2%), 88.9% (95% CI 79.3%–95.1%), 91.2% (95% CI, 76.3%–98.1%), and 86.8% (95% CI, 71.9%–95.6%), respectively (Table 3).

3.6. Comparison of image quality score by segments

In the TS images, the head ($P = .013$) and the anterior ribs and sternum ($P = .02$) had significantly lower image quality scores compared with the cervical vertebrae (Table 4). The posterior rib had a significantly lower score compared with the cervical ($P < .001$), thoracic ($P = .005$), and lumbar spine ($P = .001$) and the pelvis ($P = .010$) (Table 4).

3.7. Intraclass correlation coefficients

Intraclass correlation coefficients (ICC) were used to evaluate the inter-observer agreement between readers and were all found to be excellent: ICC, 0.898 without TS; ICC, 0.907 with TS.

3.8. False-positive lesions

A total of 17 FP lesions were observed by the three readers. The main causes of FP were osteoarthritis for 12 lesions, longitudinal

displacement of the vertebral endplate between the original and follow up CT scans in 4 lesions, and progression of osteoporosis in 1 lesion. Of 17 FP lesions, 9 lesions were in the spine, 6 lesions in the pelvis, and 2 lesions in the femoral head. Ten of 17 FP lesions were mistaken for osteolytic lesions, 6 lesions were mistaken for osteoblastic, and 1 lesion was mistaken for a mixed type lesion.

Subtraction artifacts and benign changes on the temporal subtraction images are shown in Figure 6.

3.9. Difference in sensitivity depends on the type of bone metastasis

The pooled sensitivity for the detection of bone metastases was 73.8% (31 of 42) for lytic type, 82.1% (32 of 39) for sclerotic type, 100% (15 of 15) for mixed type, and 0% (0 of 39) for intertrabecular type.

3.10. Reading time

Mean reading time for with TS was 246.8 ± 199.2 seconds, which was not significantly lower, but a trend was observed in comparison to the reading time for without TS (258.1 ± 152.7 seconds; $P = .552$).

Table 3
Segment-based and patient-based sensitivity, specificity, accuracy, positive predictive value, and negative predictive value.

Segment-based	Without TS (%)		With TS (%)	
	Without TS (%)	With TS (%)	Without TS (%)	With TS (%)
Sensitivity	54.4 [95% CI, 43.6–65.0%]	66.7 [95% CI, 55.9–76.3%]	66.7% [95% CI, 49.0–81.4%]	86.1% [95%CI, 70.5–95.3%]
Specificity	98.7 [95% CI, 97.4–99.5%]	98.9 [95% CI, 97.7–99.6%]	91.7% [95%CI, 77.5–98.2%]	91.7% [95%CI, 77.5–98.2%]
Accuracy	92.6 [95% CI, 90.3–94.5%]	94.4 [95% CI, 92.4–96.1%]	79.2% [95%CI, 68.0–87.8%]	88.9% [95%CI 79.3–95.1%]
PPV	87.5 [95% CI, 75.9–94.8%]	90.9 [95% CI, 81.3–96.6%]	88.9% [95%CI, 70.8–97.6%]	91.2% [95%CI, 76.3–98.1%]
NPV	93.1 [95% CI, 90.7–95.0%]	94.8 [95% CI, 92.7–96.5%]	73.3% [95%CI, 58.1–85.4%]	86.8% [95%CI, 71.9–95.6%]

Note - 95% CI = 95% confidence interval.
NPV=negative predictive value, PPV=positive predictive value, TS = temporal subtraction.

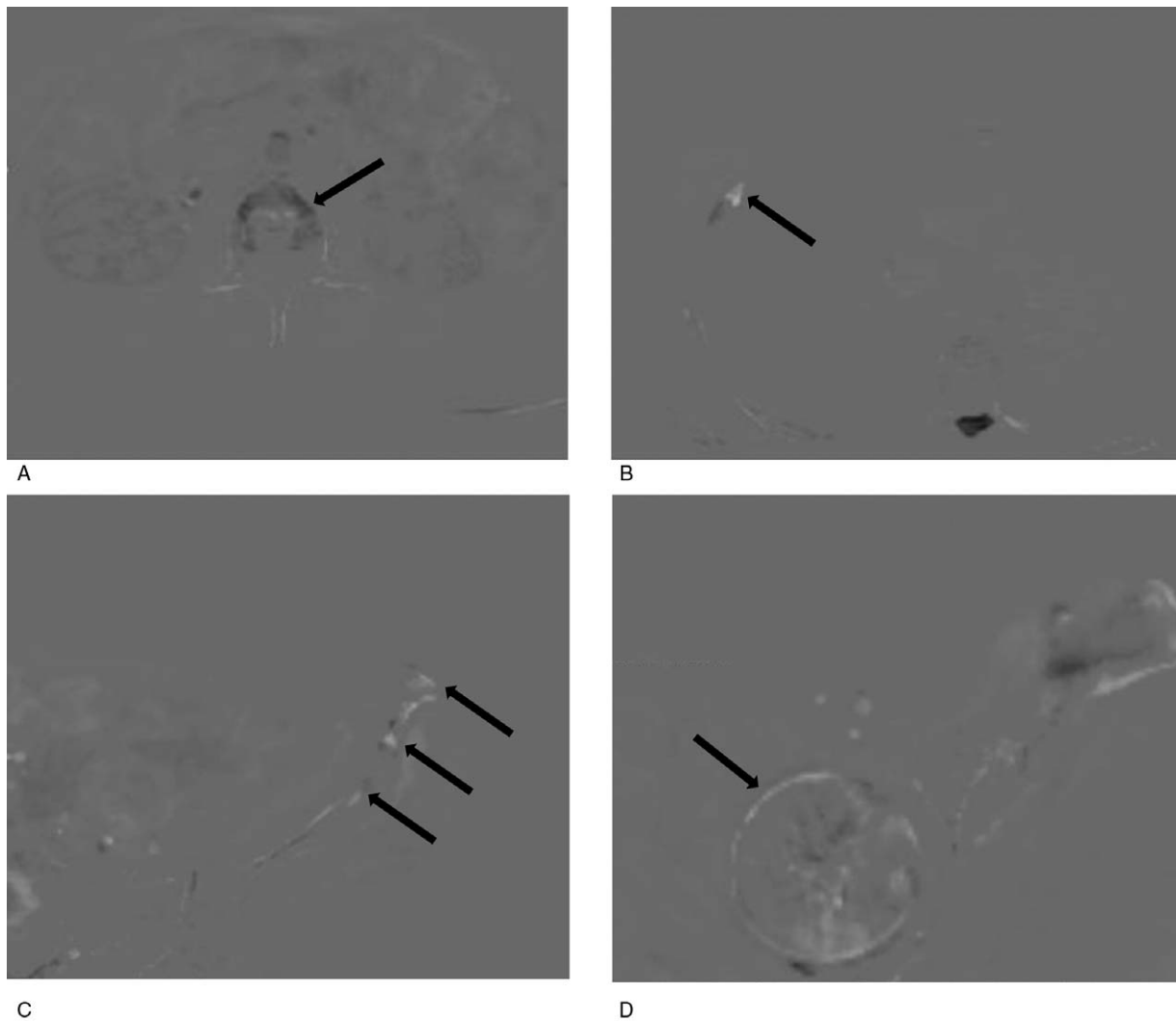


Figure 6. Subtraction artifacts and benign changes on the temporal subtraction images. (A) Image of a 62-year-old woman shows a degenerative compression fracture in the thoracic spine. (B) Image of a 58-year-old woman with breast cancer. The tips of the ribs often show band-like mild subtraction artifacts (arrow). (C,D) Images of 62-year-old woman with rectal cancer. Misalignment in the pelvis and femoral head was observed.

Table 4		
Image quality score by segment.		
Segment	Average image quality score	<i>P</i> < .001*
Head	3.8	<i>P</i> = .013 [†]
Anterior rib and sternum	3.8	<i>P</i> = .002 [‡]
Posterior rib	3.4	§
Cervical vertebrae	4.4	<i>P</i> = .013 [†]
		<i>P</i> = .002 [‡]
		§
Thoracic vertebrae	4.1	§
Lumbar vertebrae	4.2	§
Pelvis	4.1	§
Right femur	3.9	
Left femur	4.0	

* one-way analysis of variance (ANOVA).
[†] indicates significantly difference against cervical vertebrae segment.
[‡] indicates significantly difference against posterior rib segment.
[§] Posterior rib segment score is significantly lower than cervical vertebrae segment (*P* < .001), thoracic vertebrae segment (*P* = .005), lumbar vertebrae segment (*P* = .001), and pelvis segment (*P* = .010).

4. Discussion

The aim of this study was to improve the detection rate of bone metastases in low-dose and relatively thick-slice CT by using a new postprocessing method, combining LDDMM and AdVM. This study found that the additional use of TS images generated by LDDMM and AdVM can improve the detection rate of bone metastases compared to the readout with only the initial CT and follow up CT.

In this era, multi-detector CT can make the slice thickness of routine CT scan as thin as that of the source image of 3DCT, and the diagnostic accuracy of CT has been greatly improved, with a subsequent increase in the radiologist’s workload.^[32] The data obtained by CT scanning has increased remarkably, and the radiologist’s physical burden have also increased.^[33,34] In addition, there is a problem of overlooking the incidental findings in the large image section; CAD is important and expected in the near future.

Although alternative imaging modalities for the detection of bone metastases can provide better sensitivity, this study utilized

CT with PET because it is more commonly performed for the diagnosis and staging of the cancer. Bone scintigraphy was used to detect bone metastases, but it has a low detection rate for lytic metastases.^[35] Contrast-enhanced MRI is the gold standard non-invasive imaging modality for evaluating bone metastases, but it is not used routinely for follow-up in asymptomatic patients due to its limited scan area and long acquisition time. Although 18F-FDG PET/CT is useful for detecting bone metastases,^[35] sclerotic metastases may be often not detectable by FDG PET only.^[36]

5. LDDMM, AdVM, and image quality of segments

Simple subtraction between 2 CT images might cause image degradation. LDDMM is designed to cope with a large amount of deformation while retaining the topology of the object.^[17] However, the TS technique for thicker slices even with LDDMM did cause artifacts due to misregistration or partial volume effects. The AdVM algorithm was adopted to reduce the subtraction artifacts on the TS image with thick slices. The combined use of LDDMM and AdVM worked well in the current study. Using a slice thickness of up to 3.75 mm with a TS image might provide an acceptable result.

The 3.75-mm thick slice PET/CT has several disadvantages and it is challenging to generate the TS image from it. First, the PET/CT was obtained under free breathing; therefore, misregistration of chest and ribs might be expected for breathing. Second, the CT for the PET/CT was obtained with a low radiation dose; in the evaluation of bone metastases, low-radiation dose CT might not cause loss of information since bone structures can be recognized. Finally, the 3.75-mm thick slice images might have larger partial volume effects compared with the images with slice thicknesses of 1.0 mm or less. Thus, misregistration effects might also be expected. The TS image quality was lower in the anterior, posterior ribs, and the sternum compared to other bones. In the supine position, the spine does not move with breathing, unlike the chest. The lower TS image quality in anterior and posterior ribs and the sternum was probably caused by misregistration from free breathing and uncorrected partial volume effects. Despite these disadvantages, the current study indicates that TS images with PET/CT may improve the detection of bone metastases.

5.1. CT attenuation change and difference in sensitivity depending on type of bone metastasis

The amount of change in CT attenuation of TP lesions with TS readout, from initial CT to follow-up CT, was significantly greater than that of FN lesions. The principle of the TS method is subtracting the initial CT image from the follow-up CT image, emphasizing the temporal change of the CT attenuation. Therefore, bone metastases with a larger change in CT attenuation from initial CT to follow-up CT are more likely to be detected in TS images. Intertrabecular metastasis has little or no change in CT attenuation. Therefore, it was consistent that the sensitivity to detect intertrabecular bone metastases in readout using TS was 0%.

5.2. False-positive lesions

In the current study, the FP lesions were most commonly recognized in the spine. The spine has complicated geometry compared with the other bones, where the shape of the

misregistration artifacts can be more easily expected. With aging, non-metastatic deformity of the spine, including compression or spur formation, is more likely to occur compared with other bones. In our results, age-related changes such as osteoarthritis, osteophytes, sclerotic changes of vertebral body due to compression fracture, and misregistration caused by misalignment in the longitudinal direction of the endplate of the vertebral body were the main causes of FP lesions.

5.3. Reading time

Mean reading time for TS images was not significantly shorter than the time for without TS, but a trend was observed. On the contrary, there are several reports that using TS images will shorten the reading times.^[12,13,15] Possible explanations as to why reading time was not significantly shortened include that the initial CT, follow-up CT, and TS images were evaluated together in our study. Thus, the number of images was increased.

5.4. Study strengths and limitations

Our study has several strengths. Several previous studies of CAD detecting bone metastases at CT have been reported; however, they focused only vertebrae lesion^[13,14,24,37,38] or pelvis lesion.^[12] However, bone metastases can occur in any part of skeletal bone. In this study, several different body parts ranging from the head to the proximal femur were evaluated. In addition, to the best of our knowledge, there have been no studies containing intertrabecular metastases to evaluate TS. In the current study, all types of bone metastases are contained; lytic, sclerotic, mixed, and intertrabecular type. Therefore, our study has greater clinical application than the study limited to only one body part and/or one type of bone metastasis. Additionally, we conducted one-to-one age and sex matching between the patient group and control group. FP in TS tends to be marked with age-related changes of bone. By complete age- and sex- matching, the possibility of FP localization between patient group and control group is excluded. Finally, we deliberately included control patients who had no bone metastases. True-negative findings in the TS images of controls can be considered as evidence that the newly appearing CT attenuation changes were detected accurately.

Our study has several limitations. First, this study is a retrospective and single-center study. Second, selection bias was present. Patients selected were those for whom a radiologist had already dictated reports affirming the presence of bone metastases. Third, as this was a preliminary study for proof of concept, the number of patients and number of bone metastatic lesions to be assessed were small. Future investigations with larger populations will be expected. Fourth, the evaluations were solely made for the detection of bone metastasis in each session. Thus, the sensitivity for detection might be higher than that found in routine clinical practice. Fifth, regarding TS principles, our study reveals that it is difficult to detect intertrabecular metastases which present with little or no change in CT attenuation. Sixth, the TS is designed to improve lesion detection; the characterization of detected lesions as malignant or benign has yet to be accomplished. Finally, not all lesions were confirmed as bone metastases histopathologically, although efforts to confirm were made with all available information. In the clinical setting, treatment for bone metastasis does not always require pretreatment biopsy to obtain histopathologic confirmation when a primary lesion is evident.

In the future, the detectability of CAD using the Mask R-CNN or the convolutional neural network should also be evaluated.^[39–42]

In conclusion, the TS images generated by LDDMM and AdvM can significantly improve the radiologist's performance in detection of bone metastases by highlighting CT attenuation change. TS image generation from low-dose and relatively thick-slice CT by this new postprocessing algorithm is feasible and may provide non-inferior information compared to TS images generated from standard dose CT for detecting bone metastases.

Author contributions

Conceptualization: Takayuki Masui.

Data curation: Mitsuteru Tsuchiya.

Formal analysis: Mitsuteru Tsuchiya.

Investigation: Mitsuteru Tsuchiya.

Methodology: Mitsuteru Tsuchiya, Ryo Ishikawa, Hideaki Mizobe, Junta Yamamichi.

Project administration: Mitsuteru Tsuchiya.

Supervision: Takayuki Masui, Harumi Sakahara, Satoshi Goshima.

Visualization: Mitsuteru Tsuchiya.

Writing – original draft: Mitsuteru Tsuchiya.

Writing – review & editing: Takayuki Masui, Motoyuki Katayama, Yuki Hayashi, Takahiro Yamada, Kazuma Terauchi, Kenshi Kawamura, Ryo Ishikawa, Hideaki Mizobe, Junta Yamamichi.

Mitsuteru Tsuchiya orcid: 0000-0003-0915-3030.

Corrections

When originally published, Table 4 was duplicated and appeared as Table 5. The duplicate table has been removed and the reference to the table updated to Table 4.

References

- Mundy GR. Metastasis to bone: causes, consequences and therapeutic opportunities. *Nat Rev Cancer* 2002;2:584–93.
- Roodman GD. Mechanisms of bone metastasis. *N Engl J Med* 2004;350:1655–64.
- Hamaoka T, Madewell JE, Podoloff DA, et al. Bone imaging in metastatic breast cancer. *J Clin Oncol* 2004;22:2942–53.
- Coleman RE, Lipton A, Roodman GD, et al. Metastasis and bone loss: advancing treatment and prevention. *Cancer Treat Rev* 2010;36:615–20.
- Cetin K, Christiansen CF, Jacobsen JB, et al. Bone metastasis, skeletal-related events, and mortality in lung cancer patients: a Danish population-based cohort study. *Lung Cancer* 2014;86:247–54.
- Guarnieri G, Izzo R, Muto M. Current trends in mini-invasive management of spine metastases. *Interv Neuroradiol* 2015;21:263–72.
- Muindi J, Coombes RC, Golding S, et al. The role of computed tomography in the detection of bone metastases in breast cancer patients. *Br J Radiol* 1983;56:233–6.
- Groves AM, Beadsmoore CJ, Cheow HK, et al. Can 16-detector multislice CT exclude skeletal lesions during tumour staging? Implications for the cancer patient. *Eur Radiol* 2006;16:1066–73.
- Israel O, Goldberg A, Nachtigal A, et al. FDG-PET and CT patterns of bone metastases and their relationship to previously administered anti-cancer therapy. *Eur J Nucl Med Mol Imaging* 2006;33:1280–4.
- Barentsz J, Takahashi S, Oyen W, et al. Commonly used imaging techniques for diagnosis and staging. *J Clin Oncol* 2006;24:3234–44.
- Liu T, Wang S, Liu H, et al. Detection of vertebral metastases: a meta-analysis comparing MRI, CT, PET, BS and BS with SPECT. *J Cancer Res Clin Oncol* 2017;143:457–65.
- Horger M, Thaiss WM, Wiesinger B, et al. Longitudinal computed tomography monitoring of pelvic bones in patients with breast cancer using automated bone subtraction software. *Invest Radiol* 2017;52:288–94.
- Horger M, Ditt H, Liao S, et al. Automated “bone subtraction” image analysis software package for improved and faster CT monitoring of longitudinal spine involvement in patients with multiple myeloma. *Acad Radiol* 2017;24:623–32.
- Iwano S, Ito R, Umakoshi H, et al. Thoracic temporal subtraction three dimensional computed tomography (3D-CT): Screening for vertebral metastases of primary lung cancers. *PLoS One* 2017;12:e0170309.
- Sakamoto R, Yakami M, Fujimoto K, et al. Temporal subtraction of serial CT images with large deformation diffeomorphic metric mapping in the identification of bone metastases. *Radiology* 2017;285:629–39.
- 2016; American College of Radiology ACR–SPR Practice Parameter for the Performance of Computed Tomography (CT) of the Abdomen and Computed Tomography (CT) of the Pelvis.
- Ceritoglu C, Oishi K, Li X, et al. Multi-contrast large deformation diffeomorphic metric mapping for diffusion tensor imaging. *Neuroimage* 2009;47:618–27.
- Sakamoto R, Mori S, Miller MI, et al. Detection of time-varying structures by large deformation diffeomorphic metric mapping to aid reading of high-resolution CT images of the lung. *PLoS One* 2014;9:e85580.
- Tanaka T, Ishikawa R, Nakagomi K, et al. Artifacts reduction in temporal subtraction images of thick-slice CT images 2017;35:257–67. Japanese.
- Tsuchiya M, Masui T, Katayama M, et al. Temporal subtraction of relatively thick-slice CT images with large deformation diffeomorphic metric mapping and adaptive voxel matching for detecting bone metastases. *Eur Congress Radiol* 2018;doi: 10.1594/ecr2018/C-1328.
- Peller PJ. Role of positron emission tomography/computed tomography in bone malignancies. *Radiol Clin North Am* 2013;51:845–64.
- Uematsu T, Yuen S, Yukisawa S, et al. Comparison of FDG PET and SPECT for detection of bone metastases in breast cancer. *AJR Am J Roentgenol* 2005;184:1266–73.
- Israel O, Mor M, Gaitini D, et al. Combined functional and structural evaluation of cancer patients with a hybrid camera-based PET/CT system using (18)F-FDG. *J Nucl Med* 2002;43:1129–36.
- O'Connor SD, Yao J, Summers RM. Lytic metastases in thoracolumbar spine: computer-aided detection at CT—preliminary study. *Radiology* 2007;242:811–6.
- Yamaguchi T, Tamai K, Yamato M, et al. Intertrabecular pattern of tumors metastatic to bone. *Cancer* 1996;78:1388–94.
- Beg MF, Miller MI, Trouvé A, et al. Computing large deformation metric mappings via geodesic flows of diffeomorphisms 2005;61:139–57.
- Software at CIS: lddmm-volume: Namespace, Center for Image Science, Johns Hopkins University. Available at: <http://cis.jhu.edu/software/lddmm-volume/namespace.php>. Updated May 30, 2013. Accessed November 4, 2016.
- Grenander UMM. *Pattern Theory from Representation to Inference*. Oxford, England: Oxford University Press; 2007. 468–493.
- Chakraborty DP. *Observer Performance Methods for Diagnostic Imaging: Foundations, Modeling, and Applications With R-Based Examples*. 1st Edition. 2017. CRC Press, Taylor & Francis Group.
- Kim SH, Lee JM, Kim YJ, et al. Detection of hepatocellular carcinoma on CT in liver transplant candidates: comparison of PACS tile and multisynchronized stack modes. *AJR Am J Roentgenol* 2007;188:1337–42.
- Hallgren KA. Computing inter-rater reliability for observational data: an overview and tutorial. *Tutor Quant Methods Psychol* 2012;8:23–34.
- Bhargavan M, Kaye AH, Forman HP, et al. Workload of radiologists in United States in 2006–2007 and trends since 1991–1992. *Radiology* 2009;252:458–67.
- Andriole KP, Morin RL, Arenson RL, et al. Addressing the coming radiology crisis—the Society for Computer Applications in Radiology transforming the radiological interpretation process (TRIP) initiative. *J Digit Imaging* 2004;17:235–43.
- Andriole KP, Wolfe JM, Khorasani R, et al. Optimizing analysis, visualization, and navigation of large image data sets: one 5000-section CT scan can ruin your whole day. *Radiology* 2011;259:346–62.
- Chang MC, Chen JH, Liang JA, et al. Meta-analysis: comparison of F-18 fluorodeoxyglucose-positron emission tomography and bone scintigraphy in the detection of bone metastasis in patients with lung cancer. *Acad Radiol* 2012;19:349–57.

- [36] Cook GJ, Houston S, Rubens R, et al. Detection of bone metastases in breast cancer by 18FDG PET: differing metabolic activity in osteoblastic and osteolytic lesions. *J Clin Oncol* 1998;16:3375–9.
- [37] Hammon M, Dankerl P, Tsybal A, et al. Automatic detection of lytic and blastic thoracolumbar spine metastases on computed tomography. *Eur Radiol* 2013;23:1862–70.
- [38] Burns JE, Yao J, Wiese TS, et al. Automated detection of sclerotic metastases in the thoracolumbar spine at CT. *Radiology* 2013;268:69–78.
- [39] Wu E, Kong B, Wang X, et al. Residual attention based network for hand bone age assessment. 2019 IEEE 16th International Symposium on Biomedical Imaging (ISBI 2019). 2018:1158–1161.
- [40] Ye H, Gao F, Yin Y, et al. Precise diagnosis of intracranial hemorrhage and subtypes using a three-dimensional joint convolutional and recurrent neural network. *Eur Radiol* 2019;29:6191–201.
- [41] Liu X, Wang Y, Zhang H, et al. Evaluation of fractional flow reserve in patients with stable angina: Can CT compete with angiography? *Eur Radiol* 2019;29:3669–77.
- [42] Kong B, Sun S, Wang X, et al. Invasive cancer detection utilizing compressed convolutional neural network and transfer learning. *Medical Image Computing and Computer Assisted Intervention* 2018;156–64.